

The MOSDEF Survey: A Comprehensive Analysis of the Rest-optical Emission-line Properties of $z \sim 2.3$ Star-forming Galaxies¹

Jordan N. Runco,^{2*} Alice E. Shapley,² Ryan L. Sanders,^{3,4} Michael W. Topping,² Mariska Kriek,⁵ Naveen A. Reddy,⁶ Alison L. Coil,⁷ Bahram Mobasher,⁶ Brian Siana,⁶ William R. Freeman,⁶ Irene Shivaiei,^{8,4} Mojegan Azadi,⁹ Sedona H. Price,¹⁰ Gene C. K. Leung,⁷ Tara Fetherolf,⁶ Laura de Groot,¹¹ Tom Zick,⁵ Francesca M. Fornasini,⁹ Guillermo Barro¹²

¹Based on data obtained at the W.M. Keck Observatory, which is operated as a scientific partnership among the California Institute of Technology, the University of California, and the National Aeronautics and Space Administration, and was made possible by the generous financial support of the W.M. Keck Foundation.

²Physics & Astronomy Department, University of California: Los Angeles, 430 Portola Plaza, Los Angeles, CA 90095, USA

³Department of Physics, University of California, Davis, One Shields Ave, Davis, CA 95616, USA

⁴Hubble Fellow

⁵Astronomy Department, University of California, Berkeley, CA 94720, USA

⁶Department of Physics & Astronomy, University of California, Riverside, 900 University Avenue, Riverside, CA 92521, USA

⁷Center for Astrophysics and Space Sciences, University of California, San Diego, 9500 Gilman Dr., La Jolla, CA 92093-0424, USA

⁸Department of Astronomy/Steward Observatory, 933 North Cherry Ave, Rm N204, Tucson, AZ 85721-0065, USA

⁹Harvard-Smithsonian Center for Astrophysics, 60 Garden Street, Cambridge, MA, 02138, USA

¹⁰Max-Planck-Institut für Extraterrestrische Physik, Postfach 1312, Garching, 85741, Germany

¹¹Department of Physics, The College of Wooster, 1189 Beall Avenue, Wooster, OH 44691, USA

¹²Department of Physics, University of the Pacific, 3601 Pacific Ave, Stockton, CA 95211, USA

Accepted XXX. Received YYY; in original form ZZZ

ABSTRACT

We analyze the rest-optical emission-line spectra of $z \sim 2.3$ star-forming galaxies in the complete MOSFIRE Deep Evolution Field (MOSDEF) survey. In investigating the origin of the well-known offset between the sequences of high-redshift and local galaxies in the [O III] λ 5008/H β vs. [N II] λ 6585/H α (“[N II] BPT”) diagram, we define two populations of $z \sim 2.3$ MOSDEF galaxies. These include the *high* population that is offset towards higher [O III] λ 5008/H β and/or [N II] λ 6585/H α with respect to the local SDSS sequence and the *low* population that overlaps the SDSS sequence. These two groups are also segregated within the [O III] λ 5008/H β vs. [S II] λ 6718,6733/H α and the [O III] λ 4960,5008/[O II] λ 3727,3730 (O₃₂) vs. ([O III] λ 4960,5008+[O II] λ 3727,3730)/H β (R₂₃) diagrams, which suggests qualitatively that star-forming regions in the more offset galaxies are characterized by harder ionizing spectra at fixed nebular oxygen abundance. We also investigate many galaxy properties of the split sample and find that the *high* sample is on average smaller in size and less massive, but has higher specific star-formation rate and star-formation-rate surface density values and is slightly younger compared to the *low* population. From Cloudy+BPASS photoionization models, we estimate that the *high* population has a lower stellar metallicity (i.e., harder ionizing spectrum) but slightly higher nebular metallicity and higher ionization parameter compared to the *low* population. While the *high* population is more α -enhanced (i.e., higher α /Fe) than the *low* population, both samples are significantly more α -enhanced compared to local star-forming galaxies with similar rest-optical line ratios. These differences must be accounted for in *all* high-redshift star-forming galaxies – not only those “offset” from local excitation sequences.

Key words: galaxies: evolution — galaxies: high-redshift – galaxies: ISM

1 INTRODUCTION

Rest-frame optical emission-line spectroscopy is one of the most important observational tools for understanding galaxy formation

* E-mail: jrunco@astro.ucla.edu

and evolution. Such spectra provide a wealth of information about a galaxy, including its star-formation rate (SFR), dust extinction, active galactic nucleus (AGN) activity, virial and non-virial dynamics (e.g., outflows) and properties of the ionized interstellar medium such as the metallicity, electron density (n_e), and ionization parameter (U ; i.e., the ratio of ionizing photon density to hydrogen, and therefore electron, density). Accordingly, knowledge about the emission-line properties of star-forming galaxies across cosmic time is essential for understanding the evolution of the stellar and gaseous content in galaxies. It is of particular interest to study rest-optical emission-line spectra of galaxies at $z \sim 2$, which represents the epoch of peak star formation in the universe (Madau & Dickinson 2014) and a time before the modern Hubble sequence was fully in place.

In early work, Baldwin et al. (1981) showed how diagnostic diagrams measuring the intensity ratios of [O III] λ 5008/H β vs. [N II] λ 6585/H α , i.e., the “[N II] BPT diagram,” can be used to distinguish between star formation and AGN activity as the ionizing source for a galaxy. Other authors have also considered the [O III] λ 5008/H β vs. [S II] λ 6718,6733/H α diagram (originally introduced in Veilleux & Osterbrock 1987 and referred to hereafter as the “[S II] BPT diagram”) when investigating the ionization mechanism of a galaxy. Indeed, the shape of the ionizing spectrum as well as the typical ionization parameter are different in gas excited by an AGN as opposed to by hot stars. Accordingly, AGNs and star-forming galaxies occupy distinct regions within rest-optical emission-line diagrams. These diagnostic diagrams also reveal information about the physical properties of the galaxies. For example, stellar mass (M_*) and metallicity have been found to increase with decreasing [O III] λ 5008/H β and increasing [N II] λ 6585/H α along the local star-forming sequence in the [N II] BPT diagram (e.g., Masters et al. 2016).

Another diagram commonly used to describe star-forming galaxies is the [O III] λ 4960,5008/[O II] λ 3727,3730 (O_{32}) vs. ([O III] λ 4960,5008+[O II] λ 3727,3730)/H β (R_{23}) diagram. O_{32} and R_{23} are rough tracers for ionization parameter and metallicity, respectively. This diagram allows us to probe such physical quantities in star-forming galaxies (e.g. Lilly et al. 2003; Nakajima et al. 2013). For local galaxies, there is an increase in metallicity from the high excitation end (high O_{32} & R_{23}) to the low excitation tail (low O_{32} & R_{23}) on this diagram (Andrews & Martini 2013; Shapley et al. 2015).

Early studies with Keck/NIRSPEC found that the location of galaxies on the [N II] BPT diagram is redshift dependent, as galaxies with $z > 1$ are found to be offset from local Sloan Digital Sky Survey (SDSS; York et al. 2000) galaxies, showing elevated [O III] λ 5008/H β at fixed [N II] λ 6585/H α (or vice versa; e.g. Shapley et al. 2005; Erb et al. 2006; Liu et al. 2008). Based on new observations with multi-object near-infrared spectrographs on 8–10-meter class telescopes, the sample of high-redshift galaxies with measurements of the BPT diagram emission lines now numbers in the hundreds. Of note, two large surveys of the high-redshift BPT diagram include the MOSFIRE Deep Evolution Field (MOSDEF; Kriek et al. 2015) survey and the Keck Baryonic Structure Survey (KBSS; Steidel et al. 2014), which find, based on much more robust statistical evidence, that high-redshift galaxies tend to have elevated [O III] λ 5008/H β and/or [N II] λ 6585/H α compared to local galaxies (Steidel et al. 2014; Shapley et al. 2015, 2019; Sanders et al. 2016; Strom et al. 2017).

Understanding this offset in emission-line ratios is vital because we use strong rest-optical emission-lines as empirical tracers for many physical properties (e.g., gas-phase oxygen abundance

Pettini & Pagel 2004) of the interstellar medium (ISM). Due to the observed offset for $z > 1$ galaxies, it is unclear if local metallicity calibrations, e.g., Pettini & Pagel (2004), yield accurate metallicities when applied in the high-redshift universe. Therefore, it is essential to gain a complete understanding of why high-redshift galaxies have elevated [O III] λ 5008/H β and/or [N II] λ 6585/H α compared to the local SDSS sample.

There have been many proposed explanations of this systematic offset. Possible explanations include variations in physical properties of galaxies such as H II region electron densities (or proportionally pressures), density structure, H II region ionization parameter, H II region ionizing spectra at fixed metallicities, gas-phase N/O abundance ratio differences, unresolved AGN activity, and shocks (e.g. Liu et al. 2008; Brinchmann et al. 2008; Wright et al. 2010; Kewley et al. 2013; Yeh et al. 2013; Masters et al. 2014; Coil et al. 2015; Sanders et al. 2016; Steidel et al. 2016; Strom et al. 2017; Freeman et al. 2019; Kashino et al. 2019; Shapley et al. 2019; Topping et al. 2020b). Galaxy selection effects could also be potential factors in this offset (Juneau et al. 2014).

Preliminary results from the MOSDEF survey (Shapley et al. 2015; Sanders et al. 2016) suggested that the offset in emission-line ratios is primarily due to elevated N/O at fixed O/H abundance patterns in $z \sim 2.3$ galaxies relative to local ones. Studies using KBSS data (Steidel et al. 2016; Strom et al. 2017, 2018) argued for a harder ionizing spectrum at fixed nebular metallicity as the main cause of the offset while other works using the Fiber Multi-Object Spectrograph (FMOS)-COSMOS survey (Kashino et al. 2017, 2019) or local analogues of high redshift galaxies (Bian et al. 2020) attribute the observed [N II] BPT offset to a higher ionization parameter. More recent results from the MOSDEF survey using the complete MOSDEF data set now suggest a harder ionizing spectrum drives the BPT offset (Shapley et al. 2019; Sanders et al. 2020b,a; Topping et al. 2020b).

The completed MOSDEF survey provides an ideal data set of high-redshift galaxies to help explore the observed offset on the [N II] BPT diagram. This survey provides access to spectra of ~ 1500 galaxies in the $z \sim 1.4 - 3.8$ redshift range, with full spectroscopic coverage of all the emission-lines needed to complete the [N II] BPT, [S II] BPT, and O_{32} vs. R_{23} diagrams in the $z \sim 1.4 - 2.6$ redshift range.

In this work, we improve upon the previous $z > 1$ BPT offset studies based on early MOSDEF data by Shapley et al. (2015) and Sanders et al. (2016). We now have the full MOSDEF sample in hand and apply a more careful spectral energy distribution (SED) fitting method that incorporates corrections to broadband photometric measurements for rest-optical emission-line fluxes. Accordingly, we derive unbiased age and stellar mass measurements, and can conduct a more thorough and complete investigation of the emission-line ratio properties of the MOSDEF sample. As an example of the level of improvement enabled by the full MOSDEF sample, the initial work by, Shapley et al. (2015) explored the location of 53 star-forming galaxies at $1.9 \leq z \leq 2.7$ on the [N II] BPT diagram, and investigated the M_* , specific SFR (sSFR), and SFR surface density (Σ_{SFR}) of the sample. In this study, the sample increases to 180 star-forming galaxies on the [N II] BPT diagram, and we also investigate additional galaxy parameters such as the galaxy effective radius (R_e), SFR, n_e , and stellar population age. Sanders et al. (2016) investigated how a sample of 53 star-forming galaxies at $1.9 \leq z \leq 2.7$ translated from the [N II] BPT diagram to the [S II] BPT diagram and O_{32} vs. R_{23} diagram. In the current study, that number is more than doubled to 122. Our more comprehensive analysis enables a better understanding of the observed offset be-

tween the MOSDEF sample and local galaxies on the [N II] BPT diagram. Through the analysis outlined above, we aim to determine the underlying physical causes of this offset.

The paper is organized as follows. In Section 2, we briefly describe the MOSDEF survey, and review our survey sample selection and data reduction. Section 3 presents the results of this study. Section 4 discusses the results and how they relate to photoionization models. Section 5 presents a summary of key results and looks ahead to future analyses. We adopt the following abbreviations for emission-line ratios used frequently throughout the paper.

$$N2 = [\text{N II}]\lambda 6585 / H\alpha \quad (1)$$

$$S2 = [\text{S II}]\lambda\lambda 6718, 6733 / H\alpha \quad (2)$$

$$O3 = [\text{O III}]\lambda 5008 / H\beta \quad (3)$$

$$R_{23} = ([\text{O III}]\lambda\lambda 4960, 5008 + [\text{O II}]\lambda\lambda 3727, 3730) / H\beta \quad (4)$$

$$O_{32} = [\text{O III}]\lambda\lambda 4960, 5008 / [\text{O II}]\lambda\lambda 3727, 3730 \quad (5)$$

$$O3N2 = O3 / N2 \quad (6)$$

O_{32} and R_{23} have already been defined, but we include them here for completeness. All emission-line wavelengths are vacuum wavelengths. Throughout this paper, we adopt a Λ -CDM cosmology with $H_0 = 70 \text{ km s}^{-1} \text{ Mpc}^{-1}$, $\Omega_m = 0.3$, and $\Omega_\Lambda = 0.7$. Also, we assume the solar abundance pattern from [Asplund et al. \(2009\)](#).

2 METHODS

2.1 MOSDEF Sample & Ancillary Measurements

The MOSDEF survey was a 48.5-night observing program spanning multiple years (2012–2016), using the MultiObject Spectrometer For Infra-Red Exploration (MOSFIRE; [McLean et al. 2012](#)) on the 10 m Keck I telescope. The survey targets three redshift ranges: $1.37 \leq z \leq 1.70$, $2.09 \leq z \leq 2.61$, and $2.95 \leq z \leq 3.80$. These ranges are chosen to optimize the detection of strong rest-optical emission lines within windows of atmospheric transmission. There are 354, 678, and 266 galaxies that have been spectroscopically confirmed in the MOSDEF low, medium, and high-redshift ranges, respectively. The sample is H-band magnitude limited, and is located in the well-studied CANDELS and 3D-*HST* legacy fields ([Grogin et al. 2011](#); [Koekemoer et al. 2011](#); [Momcheva et al. 2016](#)): AEGIS, COSMOS, GOODS-N, GOODS-S, and UDS. The ancillary data from these fields enables us to probe other properties of the sample (e.g., galaxy size and stellar mass).

In this study, we restrict the sample to the central redshift bin, spanning the redshift range to $1.9 \leq z \leq 2.7$ to reflect the scatter between target photometric and measured spectroscopic redshifts (i.e., the fact that not all spectroscopic redshifts, when actually measured, fell precisely within the target $2.09 \leq z \leq 2.61$ window). For galaxies in this redshift range, $[\text{O II}]\lambda\lambda 3727, 3730$, $H\beta$, $[\text{O III}]\lambda\lambda 4960, 5008$, $H\alpha$, $[\text{N II}]\lambda 6585$, and $[\text{S II}]\lambda\lambda 6718, 6733$ features are captured within the J, H, and K near-IR filter wavelength ranges. For MOSFIRE, the J, H, and K filters have typical respective wavelength coverages of 1.142–1.365 μm , 1.450–1.826 μm , and

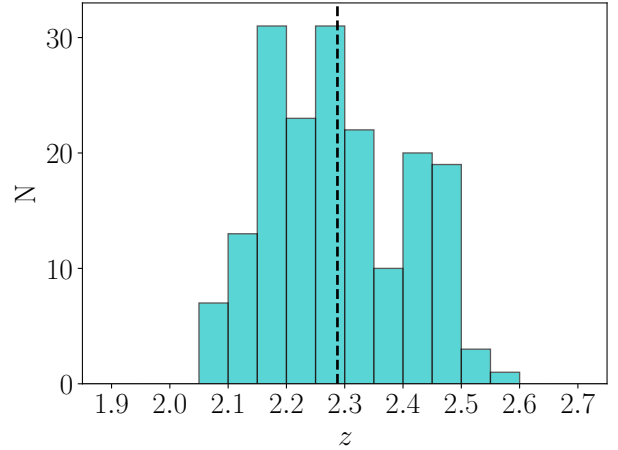


Figure 1. Redshift distribution of the 180 star-forming MOSDEF galaxies at $z \sim 2.3$ with [N II] BPT diagram classifications (i.e., $S/N \geq 3$ detections in $H\beta$, $[\text{O III}]\lambda\lambda 4960, 5008$, $H\alpha$, and $[\text{N II}]\lambda 6585$). The dashed vertical line displays the median redshift of the sample, $z_{\text{med}} = 2.29$.

1.897–2.427 μm and spectral resolutions of $R = 3000$, 3650, and 3600.

We imposed further restrictions to reach our final sample. Galaxies containing an AGN were identified and removed from the sample based on their IR colors, X-ray luminosity, or if $N2 > 0.5$ ([Coil et al. 2015](#); [Azadi et al. 2017](#); [Leung et al. 2017](#)). We also require a $S/N \geq 3$ for each emission-line in our analysis. These criteria yielded a sample of 180 galaxies for initial classification in the [N II] BPT diagram, of which 122 galaxies are additionally detected in $[\text{S II}]\lambda\lambda 6718, 6733$ and $[\text{O II}]\lambda\lambda 3727, 3730$ and have size measurements from the *Hubble Space Telescope* (*HST*). The redshift distribution of the 180 MOSDEF star-forming galaxies at $z \sim 2.3$ with [N II] BPT diagram classifications is shown in Figure 1.

We correct $H\alpha$ and $H\beta$ line fluxes for stellar Balmer absorption as described in [Kriek et al. \(2015\)](#) and [Reddy et al. \(2015\)](#). We also dust correct emission-line ratios for which the member features differ significantly in wavelength, including O_{32} and R_{23} . For such corrections, we assumed the [Cardelli et al. \(1989\)](#) dust attenuation curve and an unreddened $H\alpha/H\beta$ ratio of 2.86. In the case of emission-line ratios for which the lines are close in wavelength ($O3$, $N2$, and $S2$) dust correction was not applied.

In this study, we investigate additional galaxy photometric, spectroscopic, and structural properties for the MOSDEF sample in order to try to better understand the observed rest-optical emission-line properties. The [Hao et al. \(2011\)](#) calibration for a [Chabrier \(2003\)](#) initial mass function (IMF) and solar metallicity is used to estimate $\text{SFR}(H\alpha)$ from stellar-Balmer-absorption-corrected, dust-corrected, and slit-loss-corrected $H\alpha$ luminosities ([Reddy et al. 2015](#); [Kriek et al. 2015](#); [Shivaei et al. 2015](#)). We used the SED fitting code, FAST ([Kriek et al. 2009](#)) to obtain key stellar population parameters including stellar mass and age. For this modeling, as a default we assumed star-formation histories of the delayed- τ form, where $\text{SFR} \propto t \times e^{-t/\tau}$. Here t is the time since the onset of star formation (i.e., age), and τ is the characteristic star-formation timescale. Given the range of best-fit τ values, the meaning of absolute ages is not necessarily clear. In order to obtain a better gauge of the relative maturities of the galaxy stellar populations in our sample, we used both normalized ages (i.e., t/τ), and also the age (t) obtained from constant star formation (CSF) models.

Galaxy sizes, R_e , are taken as the F160W galaxy half-light radii from the van der Wel et al. (2014) catalog, which were estimated using single-component Sérsic profile fits to the two-dimensional light distribution of galaxies in the CANDELS and 3D-*HST* fields. We combine $\text{SFR}(H\alpha)$ and R_e to estimate the SFR surface density, Σ_{SFR} as:

$$\Sigma_{\text{SFR}} = \frac{\text{SFR}(H\alpha)}{2\pi R_e^2} \quad (7)$$

We estimate the sSFR using $\text{SFR}(H\alpha)$ and M_* , both of which are described above.

The electron density, n_e , is estimated with the [O II] and [S II] emission-line doublets using the method described in Sanders et al. (2016). In that study, the [O II] and [S II] electron densities agree within the uncertainties; both reliable tracers of the density within H II regions. [O II] is the preferred choice because the doublet typically has a higher S/N. We only use [S II] measurements when we do not have adequate [O II] data. This scenario arises for the following reasons:

(i) Low S/N. A $S/N \geq 3$ is required for each emission-line in the doublet to estimate n_e ; however, a less restrictive requirement of $S/N \geq 3$ for the overall doublet is sufficient for a galaxy to be included in the [S II] BPT and O_{32} vs. R_{23} diagrams. We only require $S/N \geq 3$ for the individual doublet members when investigating the n_e of the sample.

(ii) Rejection of the [O II] doublet based on visual inspection. Such cases occur when skylines affect the [O II] doublet but not the [S II] doublet, spurious detections, and poor fits.

We set the lower limit for n_e to be 1 cm^{-3} .

2.2 SDSS Comparison Sample

Throughout this study, we compare our high-redshift MOSDEF sample to local galaxies. For this comparison, we use archival data from the SDSS Data Release 7 (DR7; Abazajian et al. 2009). We obtain galaxy properties and emission-line measurements from the MPA-JHU DR7 release of spectrum measurements¹³. SDSS galaxies are selected within the $0.04 \leq z \leq 0.10$ redshift range. We impose similar restrictions on our SDSS sample to those applied to the MOSDEF sample by requiring that each emission-line used in the analysis has a $S/N \geq 3$. For the SDSS sample, we remove AGN using equation 1 from Kauffmann et al. (2003). Galaxies are also identified as having an AGN component if $N2 > 0.5$. These criteria result in a comparison sample of 103,422 SDSS galaxies when considering the [N II] BPT diagram alone, and 74,726 SDSS galaxies when considering galaxies with simultaneous detections across all three emission-line diagrams analyzed in this work ([N II] BPT, [S II] BPT, and O_{32} vs. R_{23}).

3 RESULTS

3.1 The [N II] BPT Diagram

We start by investigating the locations of $z \sim 2.3$ star-forming galaxies in the [N II] BPT diagram based on the complete MOSDEF sample (Figure 2). We include the 180 galaxies with $\geq 3\sigma$ detections for all four emission-lines ($H\beta$, [O III] $\lambda\lambda 4960, 5008$, $H\alpha$, and [N II] $\lambda 6585$) and the corresponding SDSS sample with the same

four emission-lines detected. Similar to previous MOSDEF studies (e.g. Shapley et al. 2015; Sanders et al. 2016; Shapley et al. 2019; Topping et al. 2020b) and other studies from the literature (e.g., Shapley et al. 2005; Erb et al. 2006; Steidel et al. 2014), there is a systematic offset observed for the high-redshift MOSDEF sample from the local sequence (Figure 2). The MOSDEF galaxies appear on average to be shifted towards the AGN region of the diagram with elevated N2 and/or O3 values, with some galaxies on the AGN side of the Kauffmann et al. (2003) AGN/SF boundary. There are even a small number of galaxies past the maximum starburst line from Kewley et al. (2001) as well.

To search for any biases in the sample based on the $\geq 3\sigma$ detection requirement in all four [N II] BPT lines, we construct spectral stacks for all MOSDEF galaxies at $1.9 \leq z \leq 2.7$ with $H\alpha$ emission detected at $S/N \geq 3$. There are four spectral stacks, divided into bins of stellar mass (see Sanders et al. 2018 for a full description of the method for constructing composite spectra). The emission-line ratios measured from stacked spectra follow the distribution of data-points measured from MOSDEF galaxies with individual detections in all [N II] BPT lines. Therefore, the sample of individual detections seems to represent the parent $z \sim 2.3$ MOSDEF data set with minimal bias. The four stacks, similarly to the individually detected galaxies, are offset from the local SDSS sample with elevated N2 and/or O3 values.

3.2 Dividing the $z \sim 2.3$ Sample in the [N II] BPT Diagram

Figure 2 shows that on the [N II] BPT diagram, part of the MOSDEF sample sits on or near the local SDSS sequence, while the remainder of the galaxies lie off the SDSS sequence and are shifted towards the local AGN region. We now investigate if the location of a high-redshift galaxy – either on or offset from the local SDSS sequence – is connected with other physical properties of the galaxy. For this analysis, we examine how galaxies on the [N II] BPT diagram populate the [S II] BPT and O_{32} vs. R_{23} diagrams, and therefore require the sample to have $\geq 3\sigma$ detections for all emission-lines on these diagrams: [O II] $\lambda\lambda 3727, 3730$, $H\beta$, [O III] $\lambda\lambda 4960, 5008$, $H\alpha$, [N II] $\lambda 6585$, and [S II] $\lambda\lambda 6718, 6733$. There are 123 MOSDEF galaxies that meet this criterion. One galaxy was removed because it does not have a R_e measurement, which brings the final sample to 122 MOSDEF galaxies.

For this analysis, we split the final sample of 122 galaxies into two groups using the functional form presented in Shapley et al. (2015), and adjusting the y-intercept so that our sample is divided in half. The equation used to split the MOSDEF sample into two groups of 61 galaxies each is

$$\log([O III]/H\beta) = \frac{0.67}{\log([N II]/H\alpha) - 0.20} + 1.065 \quad (8)$$

The new curve is 0.055 dex lower in [O III] $\lambda 5008/H\beta$ compared to equation 1 in Shapley et al. (2015). This splitting of the sample on the [N II] BPT diagram is shown in the upper left panel of Figure 3, where galaxies above the curve are indicated with blue symbols and those below with red symbols. Hereafter, we refer to the galaxies above the curve on the [N II] BPT diagram as the *high* sample, and the group below the curve as the *low* sample, following the nomenclature in Topping et al. (2020b). We plot the two samples on both the [S II] BPT diagram (upper right panel of Figure 3) and the O_{32} vs. R_{23} diagram (bottom panel of Figure 3). We also include binned median lines for both the *high* (blue) and *low* (red) populations. These binned medians are binned by $\log_{10}(O3N2)$ for the [N II] BPT diagram, $\log_{10}(O3) - \log_{10}(S2)$

¹³ <https://wwwmpa.mpa-garching.mpg.de/SDSS/DR7/>

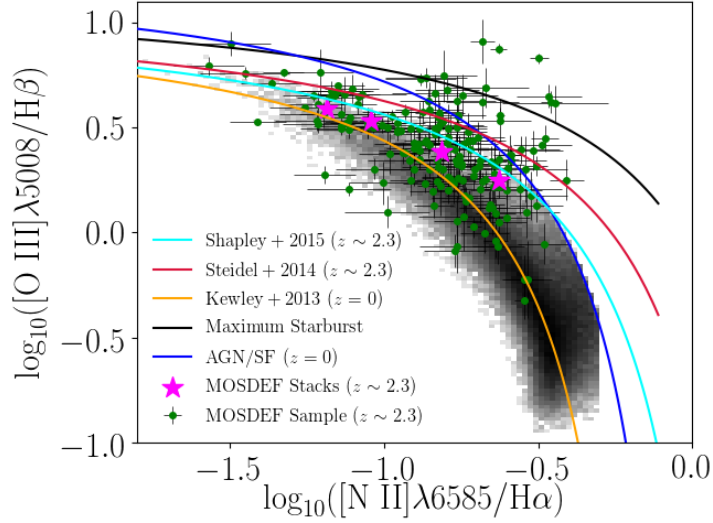


Figure 2. [N II] BPT diagram. Green points indicate $1.9 \leq z \leq 2.7$ MOSDEF galaxies with $S/N \geq 3$ for all four plotted emission-lines. Large magenta stars represent measurements of stacks from composite spectra, binned by stellar mass, for $1.9 \leq z \leq 2.7$ MOSDEF galaxies. The grayscale 2D histogram indicates local SDSS galaxies. The cyan curve is the fit to the MOSDEF sample from Shapley et al. (2015). The orange curve is a fit to the $z \sim 0$ star-forming locus (Kewley et al. 2013). The red curve is the best fit to the $z \sim 2.3$ galaxies from the Keck Baryonic Structure Survey (KBSS; Steidel et al. 2014). The black curve is the maximum starburst line from Kewley et al. (2001). The blue curve is the empirical AGN/star-forming galaxy dividing line from Kauffmann et al. (2003).

for the [S II] BPT diagram, and $\log_{10}(O_{32}) + \log_{10}(R_{23})$ for the O_{32} vs. R_{23} diagram. The binning schemes above were adopted because they divide our sample into subgroups segregated roughly along the local star-forming sequence. For both the *high* and *low* samples, each of which contain 61 galaxies, there are four equally sized bins (three bins of 15 galaxies and one bin of 16).

For completeness, we checked for potential bias between the smaller sample of 122 galaxies with detections across all three emission-line diagrams and the parent sample of 180 galaxies defined based on detections in the [N II] BPT diagram alone. Of the 58 galaxies that were removed, 32 are above the curve dividing our sample (Equation 8) and 26 are below it on the [N II] BPT diagram. Because these two groups are approximately equal in size, we can expect that the smaller subset with [O II] and [S II] also detected (122 galaxies) has approximately the same average BPT offset as the larger [N II] BPT only sample (180 galaxies). Therefore, we can conclude that the cuts to create the sample of 122 galaxies with detections across all three emission-line diagrams do not introduce biases when compared to the larger parent sample of 180 galaxies.

3.2.1 Division in the Other Diagrams

We find separation between the *high* and *low* samples on both the [S II] BPT and O_{32} vs. R_{23} diagrams. For the [S II] BPT diagram, the *high* sample has a systematically higher S2 at fixed O3 (or vice versa). For the O_{32} vs. R_{23} diagram, the *high* sample has a systematically higher R_{23} value at fixed O_{32} .

Our new results on the [S II] BPT and O_{32} vs. R_{23} diagrams update the early MOSDEF results from Sanders et al. (2016). In this earlier work, based on a significantly smaller sample of only 53 galaxies, subsamples split in the [N II] BPT diagram were found to be well mixed in the [S II] BPT and O_{32} vs. R_{23} diagrams. In contrast, our results are consistent with those of Strom et al. (2017), based on the KBSS survey. In that study, the sample was split into two groups based on [N II] BPT diagram location – large and small offset from the local SDSS sequence. These subsamples were found

to remain separated on the [S II] BPT diagram. Strom et al. (2017) did not investigate if this segregation remained on the O_{32} vs. R_{23} diagram. Section 4 contains a more in-depth comparison with the results from Strom et al. (2017) and a discussion of the implications for the underlying causes of the observed shift in the high-redshift [N II] BPT diagram.

3.2.2 Physical Properties of the Galaxies

The fact that there is a segregation in all three plots in Figure 3 implies that there are some key differences between galaxies offset from the local SDSS sequence and galaxies that overlap with it. We now investigate several galaxy physical properties to uncover any differences between the galaxies that fall into these two categories. In this study, as described in Section 2.1, we focus on: M_* , $\log(t/\tau)$ of the stellar population inferred from a delayed- τ star formation model, t of the stellar population assuming a constant star formation history, $SFR(H\alpha)$, $sSFR$, Σ_{SFR} , R_e , and n_e . We have measurements of these properties for all 122 galaxies in the sample except for n_e . As discussed in Section 2.1, a more stringent requirement of a $S/N \geq 3$ for each component of the [O II] or [S II] doublets is needed to estimate n_e while a $S/N \geq 3$ for the combined doublet is needed to be plotted on the [S II] BPT and O_{32} vs. R_{23} diagrams. Accordingly, while our fiducial sample for analysis contains 122 galaxies, only 90 of them (44 *high* and 46 *low*) have reliable n_e estimates.

We show how the *high* and *low* samples divide in the space of each of these parameters using histograms, marking the median value of the parameter with solid lines for each *high* and *low* population (Figure 4). Showing the data in this format clearly highlights how the *high* and *low* samples separately distribute in each of the galaxy parameters and, accordingly, which of the galaxy parameters are correlated with the location of galaxies on the [N II] BPT diagram. The median values for the *high* and *low* populations are listed with 1σ uncertainties derived from bootstrap resampling in Table 1. We also list the probabilities, based on the Kolmogorov-Smirnov

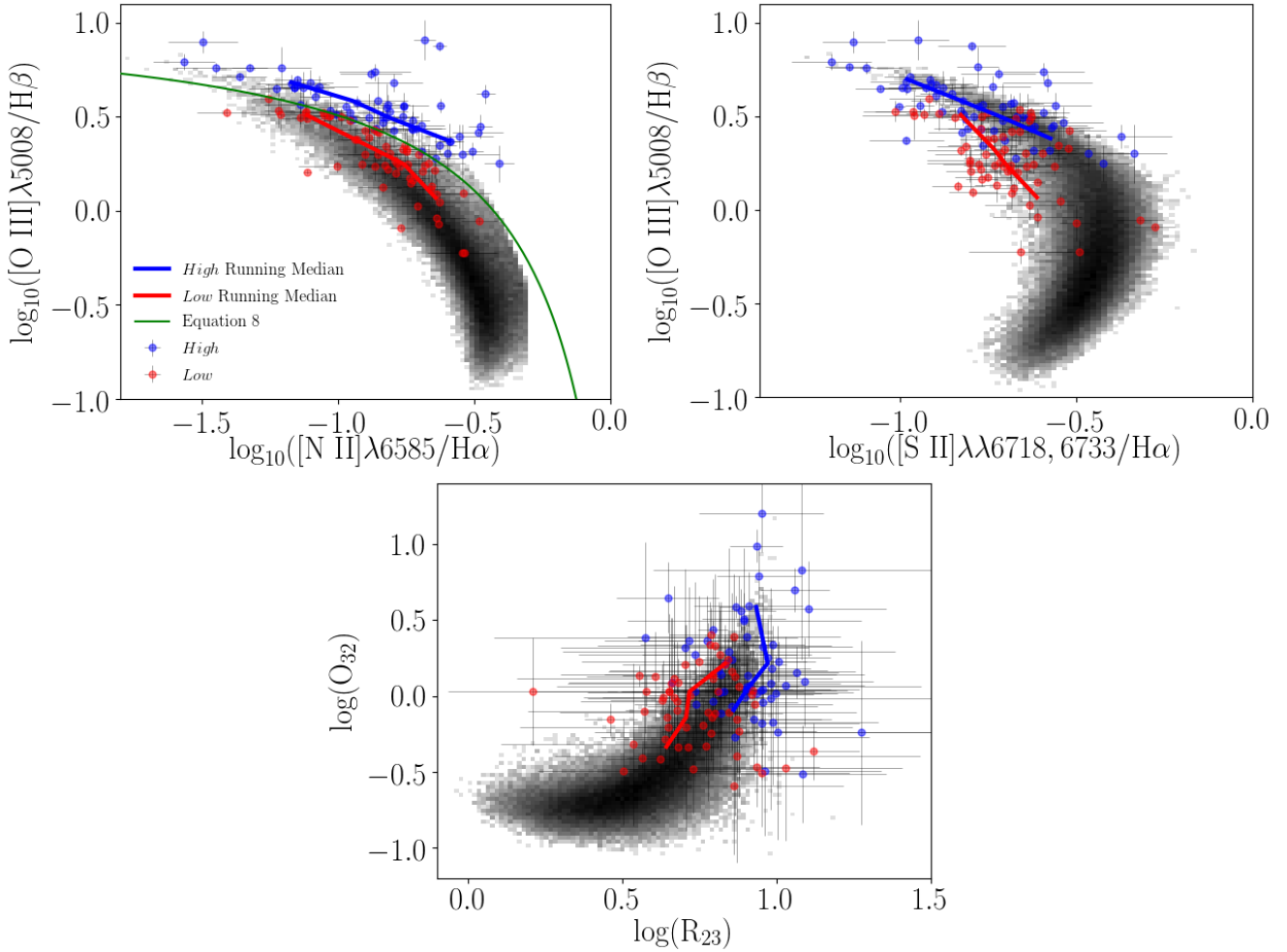


Figure 3. The sample of 122 MOSDEF galaxies that have $\geq 3\sigma$ detections in $[\text{O II}]\lambda\lambda 3727, 3730$, $\text{H}\beta$, $[\text{O III}]\lambda\lambda 4960, 5008$, $\text{H}\alpha$, $[\text{N II}]\lambda 6585$, and $[\text{S II}]\lambda\lambda 6718, 6733$. Top left: we modify the MOSDEF fit from [Shapley et al. \(2015\)](#) by altering the y-intercept, so a curve with the same functional form splits the data set evenly into two populations. The red galaxies (*low* sample) fall close to the local SDSS sequence, while the blue galaxies (*high* sample) are shifted off the local sequence. Top right: The same two groups of data points as in the left panel. The red and blue lines indicate binned medians as described in Section 3.2. These lines show that the two groups are also separated in the $[\text{S II}]$ BPT diagram, with the *high* sample higher in S2 and/or O3 than the *low* sample. Bottom center: The same two groups of data points as in the top panels. The red and blue lines again indicate binned medians as described in Section 3.2. The two groups are segregated in the O_{32} vs. R_{23} diagram as well, with the *high* sample having a higher median R_{23} values at fixed O_{32} where there is overlap in O_{32} .

(K-S) test, of the null hypothesis that the *high* and *low* samples are drawn from the same parent distribution.

While the distributions of the *high* and *low* samples significantly overlap for some galaxy parameters, there are several parameters for which the *high* and *low* distributions are measurably offset in the median and spread. These results indicate that *high* sample of MOSDEF galaxies tend to have a smaller R_e and M_* , but a larger sSFR and Σ_{SFR} compared to the *low* sample. We also note that even though R_e , sSFR, and Σ_{SFR} are correlated with M_* , at fixed M_* the *high* sample is still found to be smaller with larger sSFR and Σ_{SFR} values compared to the *low* sample. The variation in median Σ_{SFR} between the two samples can be attributed to the difference in median R_e . At fixed size, the median $\text{SFR}(\text{H}\alpha)$ values for the *high* and *low* populations agree within the uncertainties. With smaller significance, the *high* sample is also younger (smaller median t/τ and CSF t). We find no mutual correlation for either n_e or SFR with the the location of galaxies on the $[\text{N II}]$ BPT diagram.

4 DISCUSSION

4.1 Comparison with Previous Work

We have divided the $z \sim 2.3$ MOSDEF sample according to location in the $[\text{N II}]$ BPT diagram. When separated in this manner, our sample also shows segregation in the $[\text{S II}]$ BPT and O_{32} vs. R_{23} diagrams. These results update earlier MOSDEF work ([Shapley et al. 2015](#); [Sanders et al. 2016](#)), and are in agreement with more recent MOSDEF studies (e.g., [Shapley et al. 2019](#); [Topping et al. 2020b](#)). Our findings for the population segregation on the $[\text{S II}]$ BPT diagram are also in agreement with those of [Strom et al. \(2017\), in which a similar segregation in the \$\[\text{S II}\]\$ BPT diagram is found for \$z \sim 2.3\$ star-forming galaxies from the KBSS survey when separated by \$\[\text{N II}\]\$ BPT location. \[Strom et al. \\(2017\\) did not consider the relative positions of the KBSS equivalent of our *high* and *low* galaxies on the \\$\text{O}_{32}\\$ vs. \\$\text{R}_{23}\\$ diagram. However, these authors do show how photoionization models with different input parameters \\(i.e., varying ionizing spectrum at fixed nebular metallicity\\) vary\]\(#\)](#)

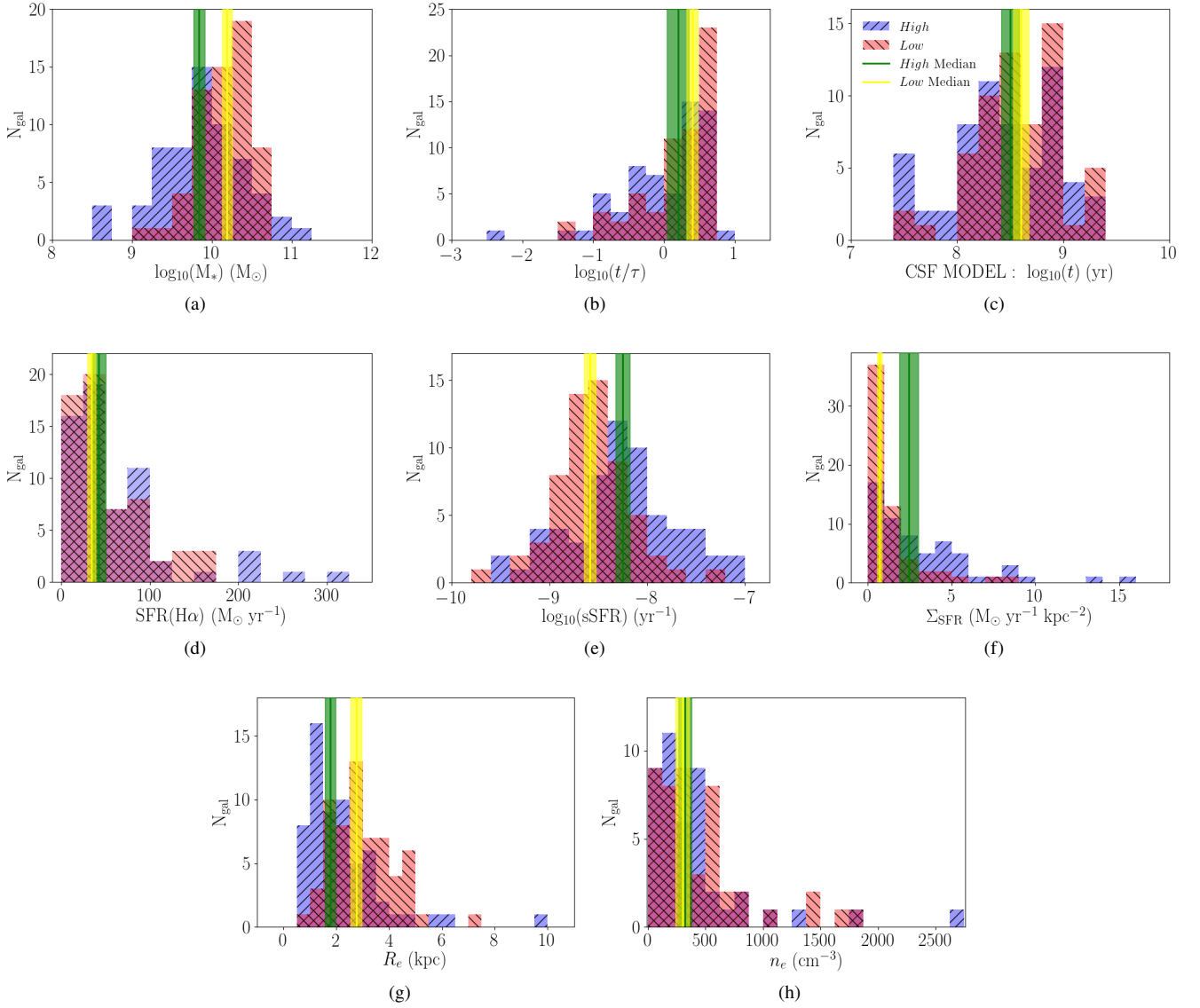


Figure 4. Distribution of physical properties for the 122 galaxy MOSDEF sample shown in Figure 3 where the blue and red bins correspond to the *high* and *low* samples, respectively. The green lines are the median values for the *high* population, while the yellow lines are the median values for the *low* population. The median values with uncertainties for both populations are given in Table 1. The following galaxy properties are shown: (a) M_* , (b) $\log(t/\tau)$ of the stellar population using a delayed- τ star formation model, (c) t of the stellar population assuming a constant star formation history, (d) $\text{SFR}(\text{H}\alpha)$, (e) sSFR , (f) Σ_{SFR} , (g) R_e , and (h) n_e estimated from the [O II] or [S II] doublet emission-lines. We find that the median M_* , sSFR , Σ_{SFR} , and R_e differ significantly based on their location in the [N II] BPT Diagram, while the other properties are the within the uncertainties of each other.

across the O_{32} vs. R_{23} parameter space. Specifically, it is shown that models with harder ionizing spectra at fixed nebular metallicity are offset towards higher R_{23} at fixed O_{32} . Strom et al. (2017) additionally show that models with harder ionizing spectra produce higher O3 at both fixed S2 and N2. These separations are at least qualitatively similar to that observed between our *high* and *low* samples.

The suggested implication of these segregations on both [S II] BPT and O_{32} vs. R_{23} diagrams is a harder ionizing spectrum at fixed O/H, relative to local galaxies (e.g., Strom et al. 2017; Shapley et al. 2019; Topping et al. 2020b). A harder ionizing spectrum at fixed nebular metallicity in $z \sim 2.3$ galaxies may arise due to α -enhancement (i.e., super-solar O/Fe values) in the massive stars exciting the ionized gas in star-forming regions. Such abundance

patterns may arise naturally in high-redshift galaxies, given the young median ages of their stellar populations (e.g., Steidel et al. 2016; Sanders et al. 2020a; Topping et al. 2020b).

We have also shown in Figure 4 that the *high* sample is associated with more compact (i.e., smaller R_e and higher Σ_{SFR}), and intense (i.e., higher sSFR) star formation than the *low* sample. These differences between the two populations exist at fixed stellar mass as well. It will be important to explore the links between these global galaxy properties and the abundance patterns of massive stars using realistic galaxy formation simulations (e.g., FIRE-2; Hopkins et al. 2018).

Median Values for Physical Properties of the *High* and *Low* Samples

Physical Property (1)	<i>High</i> Median (2)	<i>Low</i> Median (3)	p-value (4)	Statistical significance (σ) (5)
$\log_{10}(M_*/M_\odot)$	9.84 ± 0.07	10.19 ± 0.06	0.0040	2.9σ
$\log_{10}(t/\tau)$	0.20 ± 0.16	0.40 ± 0.08	0.2480	1.2σ
CSF $\log_{10}(t/\text{yr})$	8.50 ± 0.08	8.60 ± 0.07	0.1671	1.4σ
SFR($H\alpha$) ($M_\odot \text{ yr}^{-1}$)	42.7 ± 7.5	34.3 ± 4.9	0.7923	0.3σ
sSFR (yr^{-1})	-8.25 ± 0.07	-8.58 ± 0.06	0.0002	3.7σ
Σ_{SFR} ($M_\odot \text{ yr}^{-1} \text{ kpc}^{-2}$)	2.45 ± 0.56	0.70 ± 0.15	0.0002	3.7σ
R_e (kpc)	1.77 ± 0.20	2.75 ± 0.21	0.00004	4.1σ
n_e (cm^{-3})	322 ± 58	300 ± 59	0.5341	0.6σ

Table 1. Col. (1): Physical property of the galaxies in the sample shown in Figure 4. Col. (2): Median value with uncertainty of the *high* sample. Col. (3): Median value with uncertainty of the *low* sample. Col. (4): Two-tailed p-value, based on the K-S test, estimating the probability that the null hypothesis can be rejected. Col. (5): Statistical significance (i.e. the σ value) that the p-value corresponds to.

4.2 Comparison with Photoionization Models

4.2.1 Modeling Methodology

We use photoionization models to explain simultaneously the joint distributions of *high* and *low* galaxies in the [N II] and [S II] BPT and O_{32} vs. R_{23} diagrams. For this analysis, we use a combination of the code Cloudy (v17.01; [Ferland et al. 2017](#)) and the Binary Population And Spectral Synthesis (BPASS) v2.2.1 models ([Eldridge et al. 2017](#); [Stanway & Eldridge 2018](#)). BPASS generates the spectra of model stellar populations, which we used as the input ionizing spectrum to Cloudy. We assume a constant star-formation history in the BPASS models, as constructed in [Topping et al. \(2020b\)](#). Additionally, we use stellar population models that follow a [Chabrier \(2003\)](#) IMF and set $100 M_\odot$ as the high-mass cutoff.

Using the BPASS input ionizing spectrum, Cloudy predicts the rest-optical emission-line strengths for different combinations of physical properties. For this analysis, we set the N/O abundance ratio using equation (2) in [Pilyugin et al. \(2012\)](#), use the [Asplund et al. \(2009\)](#) [S II] abundance pattern, and assume that $n_e = 250 \text{ cm}^{-3}$, which is characteristic of $z \sim 2.3$ galaxies ([Sanders et al. 2016](#); [Strom et al. 2017](#); [Harshan et al. 2020](#)). This value for n_e is slightly lower than the median values of our *high* and *low* samples; however, it is within the uncertainties of the *low* population and not significantly less than the lower limit of the *high* population median. The best-fit n_e values from this study also agree within the uncertainties with the those reported in [Sanders et al. \(2016\)](#) and [Strom et al. \(2017\)](#). In addition, we use Cloudy to estimate the contribution from the nebular continuum and added this into the BPASS stellar population models. To estimate this nebular contribution, we assume that $\log(U) = -2.5$ and $\log(Z_{\text{neb}}/Z_\odot) = -0.2$, which are typical of $z \sim 2.3$ galaxies ([Sanders et al. 2016](#)). Changing these conditions does not significantly affect the nebular continuum, which is small contribution to the overall spectrum. Therefore, adjustments to the initial parameters for the nebular continuum have minimal impact on the final model fitting ([Topping et al. 2020b](#)). As a sanity check on our models, we are able to reproduce the results from [Steidel et al. \(2016\)](#) using their initial input parameters.

For our Cloudy+BPASS model grids, we varied the following parameters: stellar metallicity (Z_*), t (i.e., age) of the stellar population assuming a constant star formation history, gas-phase oxygen abundance (Z_{neb}), and ionization parameter (U). We find that our choice of t over the range 10^7 to $10^{9.8} \text{ yr}$ ([Topping et al. 2020b](#)) has a negligible effect of the position of models on all three diagrams, so we chose a value of $10^{8.6} \text{ yr}$ because it is approximately the me-

dian t (assuming a constant star-formation history) of the $z \sim 2.3$ MOSDEF sample in this study.

In the photoionization model grids, ionization parameter and nebular metallicity range between $-3.60 \leq \log(U) \leq -1.40$ and $-1.3 \leq \log(Z_{\text{neb}}/Z_\odot) \leq 0.20$, respectively. Within the ranges of interest ($-3.40 \leq \log(U) \leq -2.40$ and $-1.00 \leq \log(Z_{\text{neb}}/Z_\odot) \leq 0.00$), these grids are finely sampled in steps of 0.02 dex. Outside of these regions, $\log(U)$ changes in steps of 0.20 dex. We also include three additional values for $\log(Z_{\text{neb}}/Z_\odot)$: 0.10 and 0.20, extending up towards higher metallicity, and -1.30 to round out the low-metallicity extreme. The stellar metallicity of the BPASS models includes discrete values of $Z_* = 0.00001, 0.0001, 0.001, 0.002, 0.003, 0.004, 0.006, 0.008, 0.01, 0.014, 0.02, \text{ and } 0.03$. We assume [Asplund et al. \(2009\)](#) solar abundance (i.e., $Z_* = 0.014$).

4.2.2 Fixed Z_* Models

In a recent MOSDEF study, [Topping et al. \(2020b\)](#) combined rest-UV and rest-optical spectra for a sample of 62 star-forming galaxies at $z \sim 2.3$ and constructed *high* and *low* samples using a similar methodology as this study (i.e. based on offset from the local sequence on the [N II] BPT diagram). Fitting composite rest-frame UV spectra from their *high* and *low* stacked spectra resulted in best-fit Z_* values of 0.001 and 0.002, respectively. Best-fit Z_{neb} and $\log(U)$ values were then based on comparing the emission-line ratios measured from the stacked spectra with those generated by the same Cloudy photoionization model described above assuming the stellar metallicities obtained from the rest-UV spectra. We do not have rest-UV spectra for the full sample of 122 galaxies in our emission-line analysis, and therefore cannot obtain tight constraints on the median Z_* for the *high* and *low* samples of this work from our rest-optical data alone. Accordingly, we adopt the best-fit Z_* values from [Topping et al. \(2020b\)](#) for our two MOSDEF populations. This is a reasonable assumption because 45/62 (73%) of the galaxies in [Topping et al. \(2020b\)](#) are in this work, and the *high* and *low* samples are reasonably well matched to the corresponding samples in [Topping et al. \(2020b\)](#).

Figure 5 shows Cloudy+BPASS photoionization models overplotted with our data, assuming Z_* values of 0.001 (left column; *high* sample) and 0.002 (right column; *low* sample). Using the solar value of $12+\log(O/H) = 8.69$ ([Asplund et al. 2009](#)), we convert $\log(Z_{\text{neb}}/Z_\odot)$ to $12+\log(O/H)$. Each curve corresponds to a different $12+\log(O/H)$ value, as indicated by color. The triangular points along each nebular metallicity curve comprise the sequence of $\log(U)$ values. The points are smallest for $\log(U) = -3.60$ and

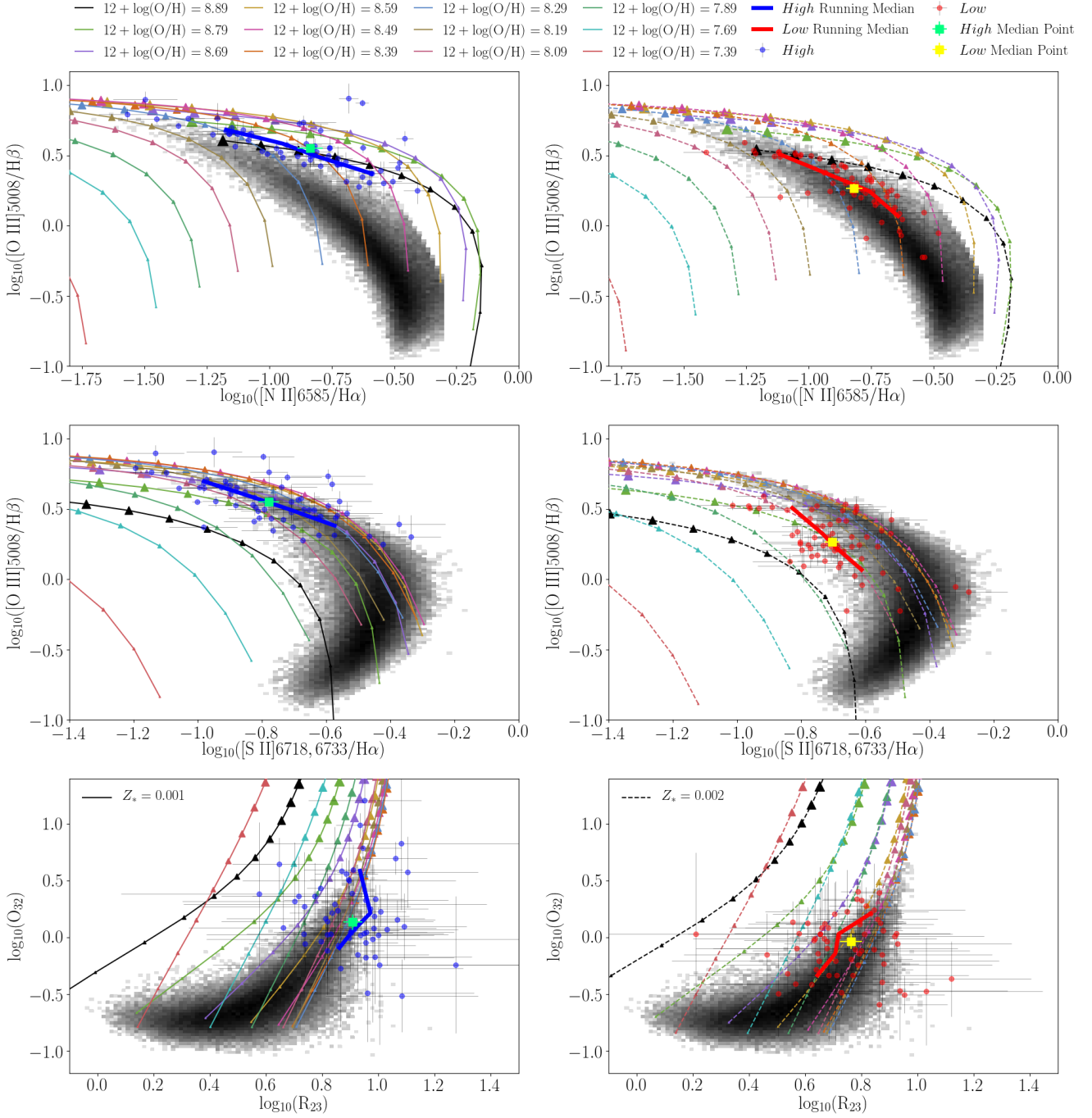


Figure 5. Left column: $Z_* = 0.001$ (solid lines). Right column: $Z_* = 0.002$ (dashed lines). Cloudy+BPASS model emission-line ratios shown on the [N II] BPT (top row), [S II] BPT (middle row), and O_{32} vs. R_{23} diagrams (bottom row). The triangle data points on the curves increase in size as $\log(U)$ increases. To avoid overcrowding, we vary $\log(U)$ in steps of 0.20 dex and have nebular metallicity range between $-0.60 \leq 12 + \log(O/H) \leq 0.20$ in 0.10 dex steps, with additional values that extend deeper into the subsolar regime included as well (-0.80 , -1.00 , and -1.30). We adopt an age of $10^{8.6}$ yr because it is the approximate median age of the MOSDEF sample (given a constant star-formation history), but the results are not sensitive to age. Also plotted are the local SDSS sample (grey 2D histogram) and the *high* (blue points) and *low* (red points) MOSDEF samples with binned medians as shown in Figure 3. The green and yellow squares, with associated uncertainties, are the median values of the *high* and *low* populations.

Single Z_* Cloudy+BPASS Median Values for Physical Properties of the <i>High</i> and <i>Low</i> Samples			
	Physical Property (1)	<i>High</i> Median (2)	<i>Low</i> Median (3)
Median Points	Z_*	0.001	0.002
	$12+\log(\text{O}/\text{H})$	$8.37^{+0.04}_{-0.04}$	$8.31^{+0.04}_{-0.02}$
	$\log(U)$	$-2.88^{+0.04}_{-0.04}$	$-3.08^{+0.02}_{-0.04}$
Large-N2	Z_*	0.002	0.003
	$12+\log(\text{O}/\text{H})$	$8.49^{+0.02}_{-0.04}$	$8.41^{+0.02}_{-0.02}$
	$\log(U)$	$-3.04^{+0.04}_{-0.04}$	$-3.26^{+0.04}_{-0.04}$
Small-N2	Z_*	0.001	0.001
	$12+\log(\text{O}/\text{H})$	$8.31^{+0.04}_{-0.04}$	$8.23^{+0.02}_{-0.02}$
	$\log(U)$	$-2.60^{+0.06}_{-0.06}$	$-2.98^{+0.02}_{-0.02}$

Table 2. Col. (1): Physical property of the sample. Col. (2): Median value with uncertainty of the *high* sample. Col. (3): Median value with uncertainty of the *low* sample. For Columns (2) & (3), the Z_* values were selected and were not obtained from fitting the data. Also, the more finely spaced grids that vary $12+\log(\text{O}/\text{H})$ and $\log(U)$ in steps of 0.02 dex were used.

largest for -1.40 , therefore, increasing in size as $\log(U)$ increases. The Cloudy+BPASS model grids are overplotted on the MOSDEF and SDSS data. The green and yellow squares on the [N II] BPT, [S II] BPT, and O_{32} vs. R_{23} diagrams indicate, respectively, the median values of the *high* and *low* samples. Uncertainties for these median values were obtained through bootstrap resampling and perturbing each resampled data point by its individual error according to a normal distribution. The sample median was calculated for each bootstrapped, perturbed sample, and then the 16th and 84th percentiles of the distribution of medians were taken as the lower and upper bounds, respectively, as the 1σ confidence interval on the plotted median value.

Using stellar metallicities of 0.001 and 0.002, respectively, for the *high* and *low* populations, we then estimate the best-fit $12+\log(\text{O}/\text{H})$ and $\log(U)$ values for the sample median data points using a χ^2 method that compares the N2, S2, O3, and O_{32} emission-line ratios between the models and data. R_{23} is not used because it is not independent of the other emission-line ratios (i.e., R_{23} can be found from a combination of O3 and O_{32}). While Figure 5 displays $12+\log(\text{O}/\text{H})$ and $\log(U)$ in large steps, we use the finer grids of 0.02 dex spacing for both physical properties when estimating the best-fit sample values. The results for the best-fit $12+\log(\text{O}/\text{H})$ and $\log(U)$ values with 1σ uncertainties from the bootstrap resampling are shown in Table 2. The corner plot showing the distributions of these two properties obtained using the bootstrapped, perturbed N2, S2, O3, and O_{32} medians are shown in the top left panel of Figure 6.

We find that both $12+\log(\text{O}/\text{H})$ and $\log(U)$ are larger for the median data point of the *high* population ($12+\log(\text{O}/\text{H}) = 8.37^{+0.04}_{-0.04}$, $\log(U) = -2.88^{+0.04}_{-0.04}$) compared to the median data point of the *low* population ($12+\log(\text{O}/\text{H}) = 8.31^{+0.04}_{-0.02}$, $\log(U) = -3.08^{+0.02}_{-0.04}$). The difference in $\log(U)$ between the two samples is more statistically significant than the difference in $12+\log(\text{O}/\text{H})$, as median values of the latter agree within the uncertainties. Because the median electron densities of the *high* and *low* sample agree within the uncertainties (see Table 1), the difference in $\log(U)$ can be attributed to the *high* population having a higher number density of ionizing

photons. This is a reasonable assumption given that the *high* sample has a lower median stellar metallicity (i.e., a harder median ionizing spectrum and greater ionizing photon production efficiency) in addition to more concentrated star formation (i.e., higher Σ_{SFR}) compared to the *low* sample. The *high* population also appears to be more α -enhanced, due to it having a lower Z_* but a higher $12+\log(\text{O}/\text{H})$ compared to the *low* population. Based on the variation of best-fit $12+\log(\text{O}/\text{H})$ and $\log(U)$ values between the *high* and *low* median data points, we conclude that quantifying both of these physical parameters, in addition to stellar metallicity (i.e., the hardness of the ionizing spectrum), is important when explaining the distribution of high-redshift galaxies in the [N II] BPT diagram. It is worth noting that we have shown the *high* population to be less massive (i.e., smaller M_*) but more metal-rich (i.e., larger $12+\log(\text{O}/\text{H})$) compared to the *low* population. This combination of physical properties is the opposite of what is expected based on results from previous studies investigating the mass-metallicity relationship (e.g. Tremonti et al. 2004; Steidel et al. 2014; Sanders et al. 2018, 2020a), which show that M_* and $12+\log(\text{O}/\text{H})$ have a positive relationship. However, the differences in mass and metallicity between the *high* and *low* samples reflect the scatter in the mass-metallicity relationship.

To check the validity of our assumption that the N/O ratio is consistent between the *high* and *low* populations, we estimate $\log(\text{N}/\text{O})$ for the sample median points based on the [N II] $\lambda 6585$ /[O II] $\lambda 3727, 3730$ tracer. We use the calibration from Strom et al. (2018) to convert from $\log([\text{N II}]\lambda 6585/[\text{O II}]\lambda 3727, 3730)$ to $\log(\text{N}/\text{O})$, and find that $\log(\text{N}/\text{O}) = -1.13 \pm 0.05$ and -1.08 ± 0.04 for the *high* and *low* samples, respectively. The consistency in $\log(\text{N}/\text{O})$ between the *high* and *low* samples validates our Cloudy+BPASS model assumptions and rules out N/O variations as the primary driver of the [N II] BPT offset. This conclusion agrees with results from other current MOSDEF studies (e.g. Shapley et al. 2019; Sanders et al. 2020a,b; Topping et al. 2020a) as well as other $z \sim 2$ studies (e.g. KBSS; Steidel et al. 2014; Strom et al. 2017, 2018).

For the most part, these results are in agreement with Topping

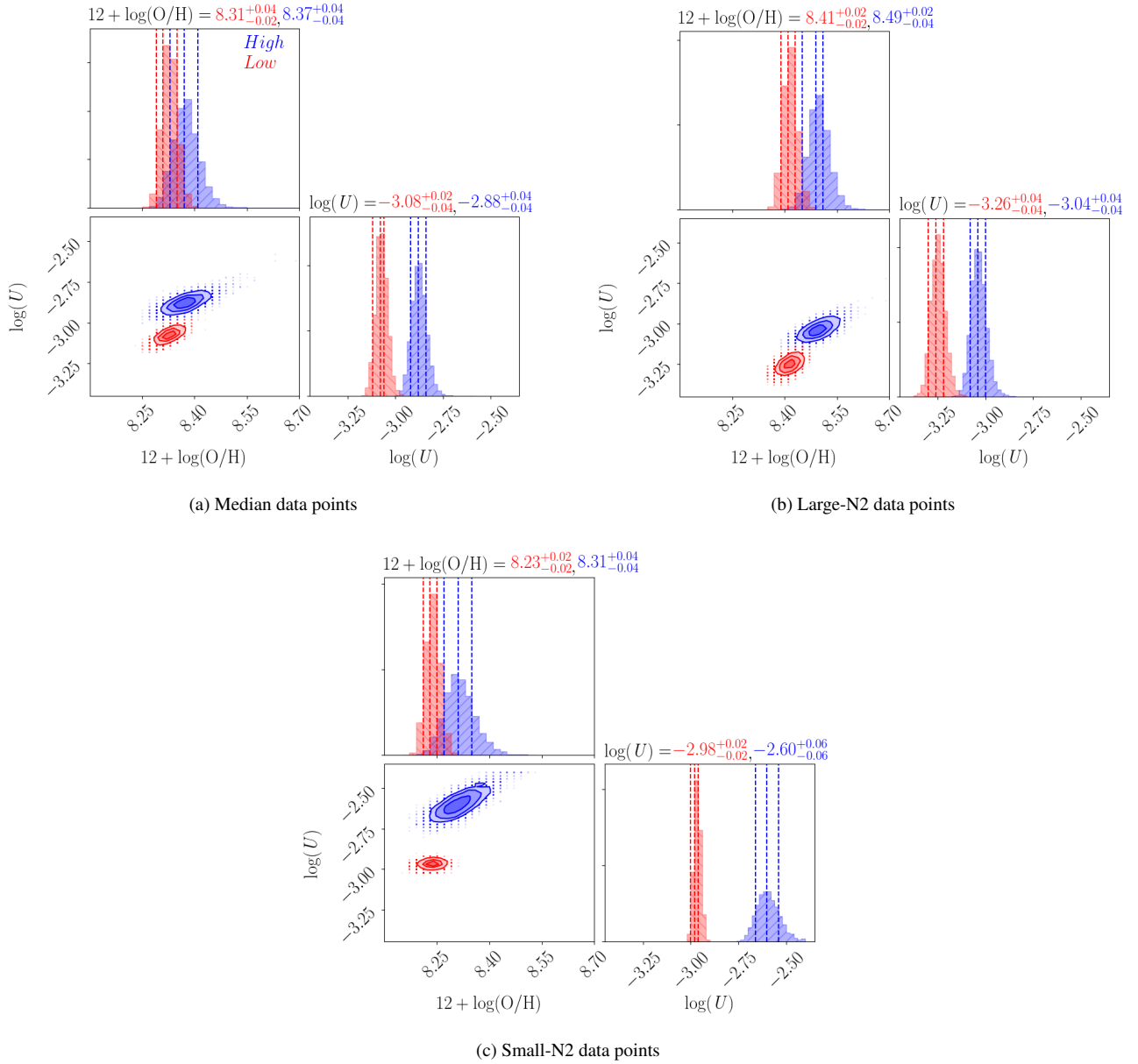


Figure 6. Corner plots comparing the distributions of $12+\log(\text{O}/\text{H})$ and $\log(U)$ for the *high* (blue) and *low* (red) MOSDEF populations. The distributions for the sample median points, i.e. green and yellow squares in Figure 5, (upper left), large-N2 endpoint of the sample binned medians (top right) and small-N2 endpoint of the sample binned medians (bottom center) are included. We assume Z_* values of 0.001 and 0.002 (median points; top left panel), 0.002 and 0.003 (large-N2 points; top right panel), and 0.001 and 0.001 (low-N2 points; bottom panel) for the *high* and *low* populations, respectively. The dashed lines on the histograms mark the median value and 1σ uncertainties (16^{th} and 84^{th} percentiles) for the distributions of $12+\log(\text{O}/\text{H})$ and $\log(U)$, and the three contours on the diagonal mark the 1 , 1.5 , and 2σ regions in the 2-D $12+\log(\text{O}/\text{H})$ - $\log(U)$ parameter space. It is shown that moving from large- to small-N2 corresponds to decreasing nebular metallicity and increasing ionization parameter. In each of the three distributions, the *high* population has a higher $12+\log(\text{O}/\text{H})$ and $\log(U)$.

et al. (2020b). The best fit $12+\log(\text{O}/\text{H})$ and $\log(U)$ values from both studies are in agreement within 1σ , except for the $\log(U)$ of the two *high* populations, which agree within 2σ . However, this study finds a larger difference in $\log(U)$ between the *high* and *low* samples, 0.20 dex, compared to Topping et al. (2020b), 0.07 dex. On the other hand, Topping et al. (2020b) find a larger variance in $12+\log(\text{O}/\text{H})$ between the two populations, 0.10 dex, compared to this study, 0.06 dex. These differences are due to the slightly different median rest-optical line ratios for the *high* and *low* populations in Topping et al. (2020b) and in the current work.

To characterize the variation of physical properties within each of our *high* and *low* populations, we apply the same methodology of finding the best-fit $12+\log(\text{O}/\text{H})$ and $\log(U)$ values, but in this case for the two endpoints of the binned medians for the *high* and *low* samples in the [N II] BPT diagram. We use the same binning method for the [N II] BPT diagram (i.e., four equally sized bins based on O3N2 strength; see Section 3.2 above for complete details on binning) when calculating the median O3, N2, S2, and O32 emission-line ratios for the endpoints of both binned median lines. Uncertainties for the line ratios of the median endpoints are esti-

mated using the same methodology of bootstrap resampling coupled with perturbation of the datapoints of individual galaxies according to their error bars, as described above. On the [N II] BPT diagram, the binned medians move primarily in the N2 direction, therefore, we refer to the endpoints of both binned median lines as “large-N2” and “small-N2”. It is important to note that the large-N2 endpoints of both *high* and *low* binned median lines have larger S2, and smaller O₃₂ compared to the small-N2 endpoints. In other words, while the binning method was not the same on all three diagrams in Figure 3 (i.e., the four bins do not necessarily contain the same galaxies), the large-N2 bins on the [N II] BPT diagram have significant overlap with (and therefore roughly correspond to) the larger-S2, and smaller-O₃₂ endpoints of the binned median lines on the [S II] BPT and O₃₂ vs. R₂₃ diagrams.

The results of Topping et al. (2020a) suggest that a positive correlation exists between N2 and Z_* (i.e., stellar metallicity tends to be higher at larger N2 values). Therefore, we vary the Z_* values that we assume for the large-N2 and small-N2 endpoints of the binned median lines accordingly. For the *low* population, we assume stellar metallicities of 0.003 and 0.001 (i.e., ± 0.001 from the median Z_*) for the large-N2 and small-N2 points, respectively. Similarly, for the *high* population, we assume stellar metallicity values of 0.002 and 0.001 for the large-N2 and small-N2 points, respectively. We do not lower the stellar metallicity of the small-N2 point of the *high* population to our next available Z_* model value (0.0001, a factor of 10 lower than the next highest Z_* value) because the results from Topping et al. (2020a) do not suggest that such a significant variation in stellar metallicity is observed. It is important to note that while we do vary Z_* in accordance with the results from Topping et al. (2020b), the best-fit $12+\log(\text{O}/\text{H})$ and $\log(U)$ for the large-N2 and small-N2 endpoints of the *high* and *low* populations do not change significantly if we use $Z_* = 0.001$ and 0.002 (i.e., the Z_* values used for the median *high* and *low* population data points). We will discuss this systematic effect of how our choice in Z_* influences the best-fit $12+\log(\text{O}/\text{H})$ and $\log(U)$ in more detail below in Sections 4.2.3 and 4.2.4.

Median $12+\log(\text{O}/\text{H})$ and $\log(U)$ values for the large-N2 and small-N2 endpoints of the *high* and *low* populations are included in Table 2. The corner plots showing the distributions of $12+\log(\text{O}/\text{H})$ and $\log(U)$ for the large-N2 and small-N2 endpoints are shown in the top right and bottom panels, respectively, of Figure 6. In both samples we find an anti-correlation between $12+\log(\text{O}/\text{H})$ and $\log(U)$ along the binned median lines. Moving from large-N2 to small-N2 (therefore also large-S2 to small-S2 and small-O₃₂ to large-O₃₂) leads to a lower $12+\log(\text{O}/\text{H})$ but a higher $\log(U)$. This anti-correlation between $\log(U)$ and $12+\log(\text{O}/\text{H})$ has been observed in local star-forming galaxies and H II regions (Pérez-Montero 2014). In addition, this trend is consistent with the idea that the high O₃₂ tail of the local sequence on the O₃₂ vs. R₂₃ diagram includes galaxies with low metallicity, and high ionization parameter (Shapley et al. 2015). Also, on the [N II] BPT diagram both stellar and nebular metallicity decrease along the local sequence (i.e., from low O3 and high N2 to high O3 and low N2).

4.2.3 Variable Z_* Models

As described above, thus far we have assumed Z_* values of 0.001 and 0.002 for the *high* and *low* population median points to match the best-fit values from modeling the rest-frame UV spectra of $z \sim 2.3$ MOSDEF galaxies (Topping et al. 2020b). While this is a reasonable assumption, we also investigate how relaxing our requirement on stellar metallicity affects the best-fit nebular metallicity and ion-

ization parameter values of the two populations. For this additional analysis, we use the same χ^2 method described above (i.e., fitting the N2, S2, O3, and O₃₂ emission-line ratios). However, we not only fit for $12+\log(\text{O}/\text{H})$ and $\log(U)$, but also treat Z_* as a free parameter. We investigate two different model grids: one that allows a small range of Z_* for the *high* and *low* samples, including the best-fit stellar metallicities from Topping et al. (2020b) for each population and those that are adjacent to the best-fit values, and a fully unrestricted method that allows all Z_* values used by the BPASS models ranging from 0.00001 to 0.03.

This analysis shows that when we relax the constraints provided by rest-UV spectra (both with limited freedom and in a fully unconstrained manner), the rest-optical emission lines tend to favor higher stellar metallicities. When we allow for limited freedom in Z_* the stellar metallicities for the *high* and *low* samples prefer the largest allowed Z_* – i.e., 0.002 and 0.003, respectively. When all stellar metallicity values are allowed, the *high* and *low* populations favor Z_* values about 4-5 times greater than those found by Topping et al. (2020b) based on fitting rest-UV spectra. These shifts demonstrate the importance of imposing external constraints from a more direct probe of massive stars and stellar metallicity, i.e., the rest-UV continuum, as opposed to relying only on a joint fit of rest-optical emission lines. We also note that, while the best-fit values of Z_* increase when stellar metallicity is allowed to vary, the *low* population still always favors a higher Z_* than the *high* population.

The best-fit $12+\log(\text{O}/\text{H})$ and $\log(U)$ values for the single- Z_* and limited freedom Z_* models are significantly consistent (i.e., within 1σ) for both the *high* and *low* populations. For the *high* sample, the best-fit values for the single- Z_* and fully unconstrained Z_* models are significantly consistent as well. For the *low* sample, only some of the best-fit values for the single- Z_* and fully unconstrained Z_* models are consistent within 1σ ; however, all values are consistent within 2σ . In addition, similar to what we find for the single- Z_* models, we find that O/H increases and $\log(U)$ decreases with increasing N2 in both free- Z_* models.

The results from this section provide guidance on which wavelength regimes best constrain different galaxy properties. Supported by other studies (e.g. Topping et al. 2020b), rest-UV spectra are essential for accurately estimating Z_* . Rest-optical spectra, even with the combination of multiple emission-line ratios, cannot constrain the stellar metallicity. At high redshift, we have shown that modeling rest-optical spectra alone will lead to overestimates of stellar metallicity relative to more accurate methods that incorporate rest-UV spectral information. However, rest-optical spectra can be used to constrain $12+\log(\text{O}/\text{H})$ and $\log(U)$. Because the best-fit values of nebular metallicity and ionization parameter vary based on which rest-optical emission-line diagram is used (see Figure 5), the combination of line ratios from multiple diagrams will increase the accuracy of the models. These parameters can even be estimated with reasonable precision without detailed knowledge of the ionizing spectrum (i.e., the metallicity of the stellar population).

4.2.4 The Importance of α -Enhancement

In summary, using rest-optical emission line ratios alone without the constraints from fitting rest-UV spectra, we infer systematically higher Z_* values for both *high* and *low* samples. At the same time, when multiple rest-optical emission lines ratios are measured (N2, S2, O3, and O₃₂), the inferred median nebular parameters ($12+\log(\text{O}/\text{H})$ and $\log(U)$) and their variation across the BPT diagram, do not depend strongly on the allowed range of Z_* . However,

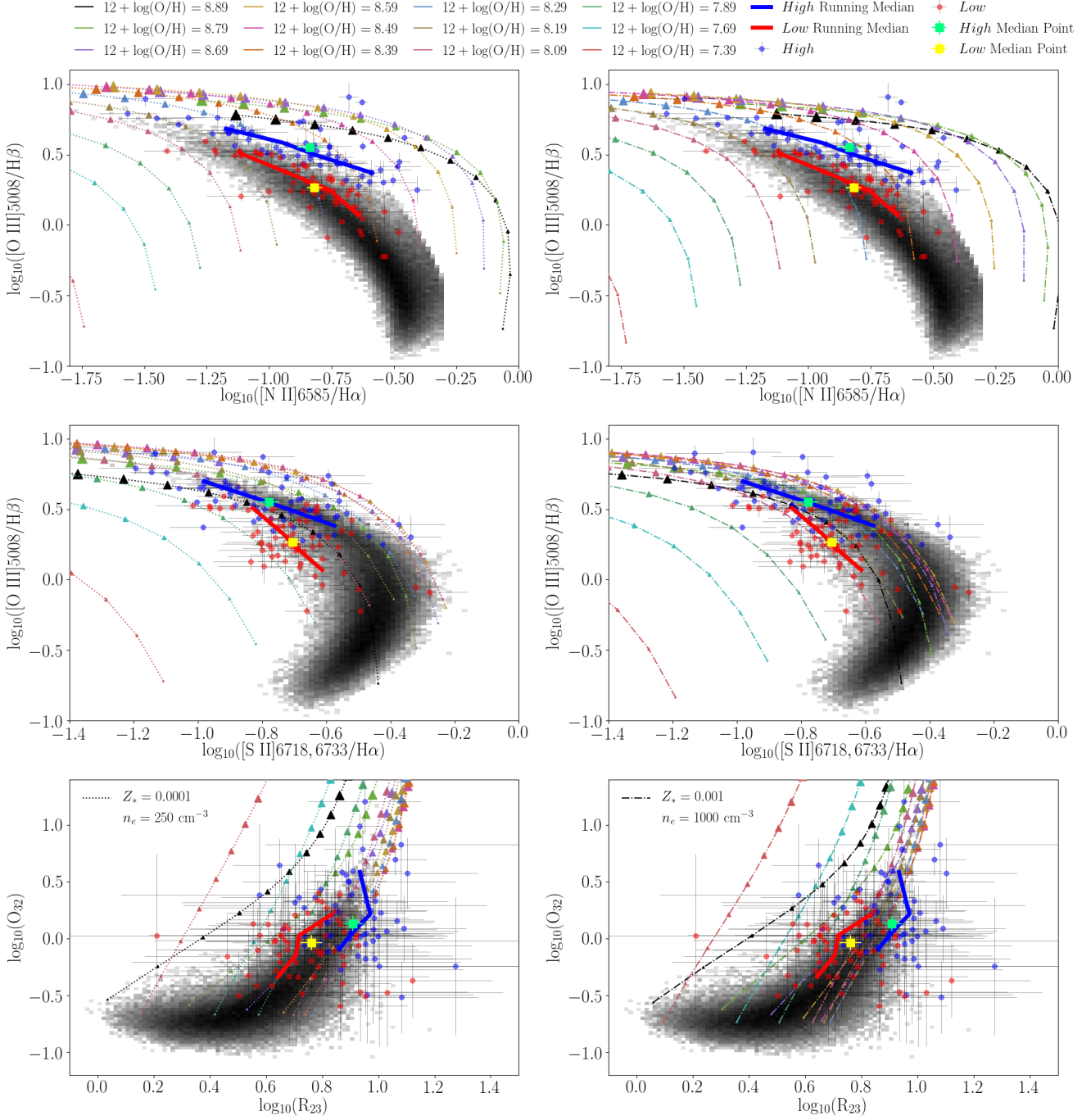


Figure 7. Left column: $Z_* = 0.0001$, $n_e = 250 \text{ cm}^{-3}$ (dotted lines). Right column: $Z_* = 0.001$, $n_e = 1000 \text{ cm}^{-3}$ (dot-dashed lines). Cloudy+BPASS model emission-line ratios shown on the [N II] BPT (top row), [S II] BPT (middle row), and O_{32} vs. R_{23} diagrams (bottom row). A comparison of these models with the corresponding panels in Figure 5 shows how raising the electron density and lowering stellar metallicity affects the predicted emission-line ratios. The correspondence between colors and symbol size and, respectively, $12+\log(O/H)$ and $\log(U)$, matches that in Figure 5. Once again, we adopt an age of $10^{8.6} \text{ yr}$ because it is the approximate median age of the MOSDEF sample (given a constant star-formation history) and include the local SDSS sample (grey 2D histogram), the *high* (blue) sample, and *low* (red) sample with binned medians as shown in Figure 3. The green and yellow squares, with associated uncertainties, are the median values of the *high* and *low* populations as shown in Figure 5. Aside from at roughly solar and supersolar nebular metallicities, a higher electron density has a minimal affect on the Cloudy+BPASS model grids and cannot reach the elevated $O3$ and O_{32} galaxies. A lower stellar metallicity is able to reach these values, suggesting that the most offset galaxies have the hardest ionizing spectrum.

the inclusion of constraints on Z_* from rest-UV fitting is essential for our understanding of the abundance patterns (i.e., α -enhancement) of $z \sim 2.3$ galaxies and we adopt the constrained values of Topping et al. (2020b) for our fiducial modeling procedure (Table 2). Because we see variation in Z_* , $12+\log(\text{O}/\text{H})$, and $\log(U)$ at the median and large- and small-N2 endpoints for the *high* and *low* samples, we conclude that constraints on all three of these physical properties are required for fully understanding the observed distribution of $z \sim 2.3$ star-forming galaxies in the [N II] BPT diagram. The importance of α -enhancement has also been highlighted by Steidel et al. (2016) and Cullen et al. (2019).

It is also important to note that while the *high* sample is more α -enhanced with a harder ionizing spectrum compared to the *low* sample, both populations are α -enhanced and both are characterized by a harder ionizing spectra when compared with their equivalents (i.e., galaxies with similar rest-optical line ratios) at low redshift. Notably, such physical differences apply to the *low* population, even though it overlaps with the local [N II] BPT sequence. Specifically, an overlap in emission-line ratios does not correspond to the same properties for the ionizing radiation field and ionized gas. Therefore, we recommend determining the location of galaxies in multiple rest-optical emission-line diagrams, as well as having some knowledge of the ionizing spectrum, when trying to identify local systems that can be used as true $z \sim 2$ analogs.

In addition, the differences between the *high* and *low* populations found in both this section and in Section 3.2.2 suggest that $z \sim 2.3$ galaxies in the *high* sample that generally have a lower Z_* with higher $12+\log(\text{O}/\text{H})$ and $\log(U)$ values are also typically smaller with higher sSFR and Σ_{SFR} values. Looking ahead, we must understand why there exists a connection between the local properties of ionized star-forming regions and the overall compactness/intensity of star formation. However, exploring this phenomenon is outside the scope of the current work.

4.2.5 Discrepancies Between Data and Models

It is worth noting that in all three diagrams in Figure 5, there are galaxies that do not lie within the Cloudy+BPASS grid space. On the [N II] BPT and [S II] BPT diagrams, there are galaxies with O3 values that exceed the extremes of the model grids. Similarly on the O32 vs. R23 diagram, we observe MOSDEF galaxies with higher R23 values than what the Cloudy+BPASS models predict. These offsets are primarily found among the *high* population. Such extreme galaxies are not specific to this study, as Strom et al. (2017) find similar discrepancies between data and models in the corresponding emission-line diagnostic diagrams.

For the Cloudy+BPASS model grids in this study, two possible solutions could be to either elevate n_e or lower Z_* . Increasing n_e has been shown to cause elevated O3 and N2 values (Kewley et al. 2013). Since the *high* population (defined by its elevated O3 and/or N2 values) also has elevated R23 values on average, increasing n_e in our Cloudy+BPASS models theoretically could push the curves to higher R23. The models in this study, which were constructed by Topping et al. (2020b), set $n_e = 250 \text{ cm}^{-3}$, which is typical of $z \sim 2.3$ galaxies in both the KBSS sample (Strom et al. 2017) and early MOSDEF work (Sanders et al. 2016). It is also comparable with the median electron densities reported in this work. The models employed in Strom et al. (2017) use $n_e = 300 \text{ cm}^{-3}$, and similarly cannot reach the highest observed O3 and R23 values in the KBSS survey.

Using $Z_* = 0.001$, we explore raising n_e to 1000 cm^{-3} in the Cloudy+BPASS models (right column of Figure 7). Comparing the

elevated electron density models with the $Z_* = 0.001$, $n_e = 250 \text{ cm}^{-3}$ scenario (left column of Figure 5) shows the differences in the predicted emission line ratios caused by isolating variations in n_e on the [N II] BPT, [S II] BPT, and O32 vs. R23 diagrams. We find that elevating n_e to such an extreme value has only a small effect on the emission-line ratios, and the models still do not encompass the galaxies observed at the highest N2, S2, O3, and R23 values.

A more promising approach is to lower the stellar metallicity. The left column of Figure 7 gives the model grids for $Z_* = 0.0001$, which reach the majority of the extreme data points. Therefore, a very low Z_* (i.e., a very hard ionizing spectrum) is the more likely than variations in n_e to be cause for these outliers.

In addition to a low Z_* , other effects may also lead to a harder ionizing spectrum (e.g., variations in the IMF slope and high-mass cutoff or AGN partially contributing to the integrated emission lines). Systematic uncertainties such as the BPASS models underpredicting the hardness of the ionizing spectrum at a given Z_* (particularly at lower values of Z_*), different star-formation histories, or uncertainties in the dust corrections applied to O32 and R23 could play a role in the observed discrepancies between models and a minority of the sample as well.

5 SUMMARY

We present results on the emission-line properties of a sample of 122 star-forming galaxies at $1.9 \leq z \leq 2.7$ from the complete MOSDEF survey with $\geq 3\sigma$ detections for the [O II] $\lambda\lambda 3727, 3730$, H β , [O III] $\lambda\lambda 4960, 5008$, H α , [N II] $\lambda 6585$, and [S II] $\lambda\lambda 6718, 6733$ emission lines. To investigate the observed systematic offset of $z > 1$ star-forming galaxies on the [N II] BPT diagram relative to local systems, the MOSDEF sample is split into the *high* (offset with elevated O3 and/or N2 values) and *low* (overlapping with the local SDSS sequence) samples. We compare the location of galaxies in both populations on the [S II] BPT and O32 vs. R23 diagrams. Additionally, we compare physical properties – SFR, M_* , R_e , sSFR, Σ_{SFR} , n_e , and t (i.e., stellar population age) – of the galaxies in both groups using additional CANDELS and 3D-HST ancillary data. Finally, we use Cloudy+BPASS photoionization models to investigate potential differences in the stellar metallicity, nebular metallicity, and ionization parameter of the *high* and *low* groups.

The main results are as follows:

(i) On the [S II] BPT and O32 vs. R23 diagrams, the *high* sample is offset on average towards higher S2 at fixed O3 (or vice versa) and higher R23 value at fixed O32, respectively, relative to the *low* sample. These results update earlier work from MOSDEF (Sanders et al. 2016) and are consistent with results from Strom et al. (2017), based on the KBSS survey.

(ii) The *high* sample has a smaller median R_e and M_* , but higher median sSFR and Σ_{SFR} compared to the *low* sample. The observed differences in R_e , sSFR, and Σ_{SFR} are present at fixed stellar mass. The *high* sample is also slightly younger in median age (t); however this age difference is not significant within the uncertainties. There is not a significant variation in SFR or n_e for the two populations. These results imply that the *high* population is associated with more concentrated and intense star formation than the *low* population.

(iii) Using photoionization models, we find that the *high* population has larger $12+\log(\text{O}/\text{H})$ and $\log(U)$ values compared to the *low* population. These conclusions hold both when we use the results from Topping et al. (2020b) and assume Z_* values of 0.001 and 0.002 for the *high* and *low* samples, respectively, as well as when we treat Z_* as a free parameter. Also, while the lower Z_*/Z_{neb} ratio

of the *high* population implies that this sample is more α -enhanced than the *low* population, both samples are significantly α -enhanced relative to local star-forming galaxies with similar emission-line ratios assuming typical local galaxies have roughly solar α/Fe . These differences in the properties of the ionizing radiation field are critical to include when describing high-redshift galaxies – even those that overlap the local emission-line sequences.

(iv) Combining the results from the median galaxy properties of the *high* and *low* samples with the Cloudy+BPASS model grids leads to the conclusion that galaxies with a harder ionizing spectrum are associated with smaller sizes and higher sSFR and Σ_{SFR} .

(v) A harder ionizing spectrum at fixed nebular metallicity is favored as one of the key drivers of the [N II] BPT offset. In this study, we find that variation in multiple physical parameters drives the variation in emission-lines in the MOSDEF sample, including Z_* , $12+\log(\text{O}/\text{H})$, and $\log(U)$. However, even in regions where the $z \sim 2.3$ galaxies overlap local ones in the space of emission-line ratios, the inferred underlying physical parameters for $z \sim 2.3$ galaxies are distinct from those of local galaxies. The full set of these parameters must be understood through modeling both rest-UV and rest-optical spectra, in order to understand the translation between empirical emission-line ratios and key physical quantities such as the gas-phase oxygen abundance.

Understanding the global properties of high-redshift galaxies using large samples at $z \sim 2.3$ is essential when comparing them with local galaxies. The use of large high-redshift samples has enabled us to discover more subtle trends in the MOSDEF data that were not found with more limited data sets (e.g. Shapley et al. 2015; Sanders et al. 2016). The work from this study has shown that galaxies with a harder ionizing spectrum also tend to be smaller in size with more intense and compact star formation. Why these factors are linked is not yet clear, and combining large $z \sim 2.3$ samples of star-forming galaxies with realistic galaxy formation simulations (e.g., FIRE-2; Hopkins et al. 2018) will be important in finding this connection.

It has also been shown in both this work and in Strom et al. (2017) that models are not yet able to reach the highest observed O3 and R₂₃ values for $z \sim 2.3$ star-forming galaxies on the [N II] BPT, [S II] BPT, and O₃₂ vs. R₂₃ diagrams. The local sequence does not reach such elevated O3 and R₂₃ values, and unlike their high redshift counterparts, do not greatly exceed the data space covered by the model grids. This discrepancy indicates a need to develop both stellar population and emission-line models that better match the now large data sets of $z \sim 2.3$ star-forming galaxies.

ACKNOWLEDGEMENTS

We thank the referee for a thorough and constructive report. We acknowledge support from NSF AAG grants AST1312780, 1312547, 1312764, and 1313171, grant AR-13907 from the Space Telescope Science Institute, and grant NNX16AF54G from the NASA ADAP program. We also acknowledge a NASA contract supporting the “WFIRST Extragalactic Potential Observations (EXPO) Science Investigation Team” (15-WFIRST15-0004), administered by GSFC. We thank the 3D-HST collaboration, who provided us with spectroscopic and photometric catalogs used to select MOSDEF targets and derive stellar population parameters. We acknowledge the First Carnegie Symposium in Honor of Leonard Searle for useful information and discussions that benefited this work. This research made

use of Astropy,¹⁴ a community-developed core Python package for Astronomy (Astropy Collaboration et al. 2013, 2018). We finally wish to extend special thanks to those of Hawaiian ancestry on whose sacred mountain we are privileged to be guests.

DATA AVAILABILITY

The data underlying this article will be shared on reasonable request to the corresponding author.

Facilities: Keck/MOSFIRE, SDSS

Software: Astropy (Astropy Collaboration et al. 2013, 2018), Corner (Foreman-Mackey 2016), IPython (Perez & Granger 2007), Matplotlib (Hunter 2007), NumPy (Oliphant 2006; van der Walt et al. 2011), SciPy (Oliphant 2007; Millman & Aivazis 2011; Virtanen et al. 2020)

REFERENCES

- Abazajian K. N., et al., 2009, *ApJS*, **182**, 543
- Andrews B. H., Martini P., 2013, *ApJ*, **765**, 140
- Asplund M., Grevesse N., Sauval A. J., Scott P., 2009, *ARA&A*, **47**, 481
- Astropy Collaboration et al., 2013, *A&A*, **558**, A33
- Astropy Collaboration et al., 2018, *AJ*, **156**, 123
- Azadi M., et al., 2017, *ApJ*, **835**, 27
- Baldwin J. A., Phillips M. M., Terlevich R., 1981, *PASP*, **93**, 5
- Bian F., Kewley L. J., Groves B., Dopita M. A., 2020, *MNRAS*, **493**, 580
- Brinchmann J., Pettini M., Charlot S., 2008, *MNRAS*, **385**, 769
- Cardelli J. A., Clayton G. C., Mathis J. S., 1989, *ApJ*, **345**, 245
- Chabrier G., 2003, *PASP*, **115**, 763
- Coil A. L., et al., 2015, *ApJ*, **801**, 35
- Cullen F., et al., 2019, *MNRAS*, **487**, 2038
- Eldridge J. J., Stanway E. R., Xiao L., McClelland L. A. S., Taylor G., Ng M., Greis S. M. L., Bray J. C., 2017, *Publ. Astron. Soc. Australia*, **34**, e058
- Erb D. K., Steidel C. C., Shapley A. E., Pettini M., Reddy N. A., Adelberger K. L., 2006, *ApJ*, **647**, 128
- Ferland G. J., et al., 2017, *Rev. Mex. Astron. Astrofis.*, **53**, 385
- Foreman-Mackey D., 2016, *The Journal of Open Source Software*, **1**, 24
- Freeman W. R., et al., 2019, *ApJ*, **873**, 102
- Grogin N. A., et al., 2011, *ApJS*, **197**, 35
- Hao C.-N., Kennicutt R. C., Johnson B. D., Calzetti D., Dale D. A., Moustakas J., 2011, *ApJ*, **741**, 124
- Harshan A., et al., 2020, *ApJ*, **892**, 77
- Hopkins P. F., et al., 2018, *MNRAS*, **480**, 800
- Hunter J. D., 2007, *Computing in Science & Engineering*, **9**, 90
- Juneau S., et al., 2014, *ApJ*, **788**, 88
- Kashino D., et al., 2017, *ApJ*, **835**, 88
- Kashino D., et al., 2019, *ApJS*, **241**, 10
- Kauffmann G., et al., 2003, *MNRAS*, **346**, 1055
- Kewley L. J., Dopita M. A., Sutherland R. S., Heisler C. A., Trevena J., 2001, *ApJ*, **556**, 121
- Kewley L. J., Dopita M. A., Leitherer C., Davé R., Yuan T., Allen M., Groves B., Sutherland R., 2013, *ApJ*, **774**, 100
- Koekemoer A. M., et al., 2011, *ApJS*, **197**, 36
- Kriek M., van Dokkum P. G., Labbé I., Franx M., Illingworth G. D., Marchesini D., Quadri R. F., 2009, *ApJ*, **700**, 221
- Kriek M., et al., 2015, *ApJS*, **218**, 15
- Leung G. C. K., et al., 2017, *ApJ*, **849**, 48
- Lilly S. J., Carollo C. M., Stockton A. N., 2003, *ApJ*, **597**, 730

¹⁴ <http://www.astropy.org>

- Liu X., Shapley A. E., Coil A. L., Brinchmann J., Ma C.-P., 2008, *ApJ*, **678**, 758
- Madau P., Dickinson M., 2014, *ARA&A*, **52**, 415
- Masters D., et al., 2014, *ApJ*, **785**, 153
- Masters D., Faisst A., Capak P., 2016, *ApJ*, **828**, 18
- McLean I. S., et al., 2012, in *Ground-based and Airborne Instrumentation for Astronomy IV*. p. 84460J, doi:10.1117/12.924794
- Millman K. J., Aivazis M., 2011, *Computing in Science & Engineering*, **13**, 9
- Momcheva I. G., et al., 2016, *ApJS*, **225**, 27
- Nakajima K., Ouchi M., Shimasaku K., Hashimoto T., Ono Y., Lee J. C., 2013, *ApJ*, **769**, 3
- Oliphant T., 2006, *NumPy: A guide to NumPy*, USA: Trelgol Publishing, <http://www.numpy.org/>
- Oliphant T. E., 2007, *Computing in Science & Engineering*, **9**, 10
- Perez F., Granger B. E., 2007, *Computing in Science & Engineering*, **9**, 21
- Pérez-Montero E., 2014, *MNRAS*, **441**, 2663
- Pettini M., Pagel B. E. J., 2004, *MNRAS*, **348**, L59
- Pilyugin L. S., Vílchez J. M., Mattsson L., Thuan T. X., 2012, *MNRAS*, **421**, 1624
- Reddy N. A., et al., 2015, *ApJ*, **806**, 259
- Sanders R. L., et al., 2016, *ApJ*, **816**, 23
- Sanders R. L., et al., 2018, *ApJ*, **858**, 99
- Sanders R. L., et al., 2020a, *MNRAS*, **491**, 1427
- Sanders R. L., et al., 2020b, *ApJ*, **888**, L11
- Shapley A. E., Coil A. L., Ma C.-P., Bundy K., 2005, *ApJ*, **635**, 1006
- Shapley A. E., et al., 2015, *ApJ*, **801**, 88
- Shapley A. E., et al., 2019, *ApJ*, **881**, L35
- Shivaei I., et al., 2015, *ApJ*, **815**, 98
- Stanway E. R., Eldridge J. J., 2018, *MNRAS*, **479**, 75
- Steidel C. C., et al., 2014, *ApJ*, **795**, 165
- Steidel C. C., Strom A. L., Pettini M., Rudie G. C., Reddy N. A., Trainor R. F., 2016, *ApJ*, **826**, 159
- Strom A. L., Steidel C. C., Rudie G. C., Trainor R. F., Pettini M., Reddy N. A., 2017, *ApJ*, **836**, 164
- Strom A. L., Steidel C. C., Rudie G. C., Trainor R. F., Pettini M., 2018, *ApJ*, **868**, 117
- Topping M. W., Shapley A. E., Reddy N. A., Sanders R. L., Coil A. L., Kriek M., Mobasher B., Siana B., 2020a, arXiv e-prints, p. [arXiv:2008.02282](https://arxiv.org/abs/2008.02282)
- Topping M. W., Shapley A. E., Reddy N. A., Sanders R. L., Coil A. L., Kriek M., Mobasher B., Siana B., 2020b, *MNRAS*, **495**, 4430
- Tremonti C. A., et al., 2004, *ApJ*, **613**, 898
- Veilleux S., Osterbrock D. E., 1987, *ApJS*, **63**, 295
- Virtanen P., et al., 2020, *Nature Methods*, **17**, 261
- Wright S. A., Larkin J. E., Graham J. R., Ma C.-P., 2010, *ApJ*, **711**, 1291
- Yeh S. C. C., Verdolini S., Krumholz M. R., Matzner C. D., Tielens A. G. G. M., 2013, *ApJ*, **769**, 11
- York D. G., et al., 2000, *AJ*, **120**, 1579
- van der Walt S., Colbert S. C., Varoquaux G., 2011, *Computing in Science & Engineering*, **13**, 22
- van der Wel A., et al., 2014, *ApJ*, **788**, 28

This paper has been typeset from a $\mathrm{T}_{\mathrm{E}}\mathrm{X}/\mathrm{L}^{\mathrm{A}}\mathrm{T}_{\mathrm{E}}\mathrm{X}$ file prepared by the author.